



HAL
open science

Sintering of a UO_2 - PuO_2 freeze-granulated powder under reducing conditions

Julie Simeon, Florent Lebreton, Laure Ramond, Florian La Lumia, Nicolas Clavier, Guillaume Bernard-Granger

► **To cite this version:**

Julie Simeon, Florent Lebreton, Laure Ramond, Florian La Lumia, Nicolas Clavier, et al.. Sintering of a UO_2 - PuO_2 freeze-granulated powder under reducing conditions. *Journal of the European Ceramic Society*, 2020, 40 (15), pp.5900-5908. 10.1016/j.jeurceramsoc.2020.07.022 . hal-02927353

HAL Id: hal-02927353

<https://hal.science/hal-02927353>

Submitted on 1 Sep 2020

HAL is a multi-disciplinary open access archive for the deposit and dissemination of scientific research documents, whether they are published or not. The documents may come from teaching and research institutions in France or abroad, or from public or private research centers.

L'archive ouverte pluridisciplinaire **HAL**, est destinée au dépôt et à la diffusion de documents scientifiques de niveau recherche, publiés ou non, émanant des établissements d'enseignement et de recherche français ou étrangers, des laboratoires publics ou privés.

1
2
3
4
5
6
7
8
9
10
11
12
13
14
15
16
17
18
19
20
21
22
23
24
25
26
27
28
29
30
31
32
33
34
35
36
37
38
39
40
41
42
43
44
45
46
47
48
49
50
51
52
53
54
55
56
57
58
59
60
61
62
63
64
65

Sintering of a UO₂-PuO₂ freeze-granulated powder under reducing conditions

Julie Simeon, Florent Lebreton, Laure Ramond, Florian La Lumia, N. Clavier[†]
& Guillaume Bernard-Granger

CEA, DES, ISEC, DMRC, Univ Montpellier, Marcoule, France

[†]ICSM, Univ Montpellier, CEA, CNRS, ENSCM, Bagnols-sur-Cèze, France

Abstract

A freeze-granulated powder made of UO₂ and PuO₂, containing 15 mol% of Pu/(U+Pu), was sintered under reducing conditions (oxygen potential of -468 kJ/mol at 1700 °C). Constructing the “grain size versus relative density” trajectory, using the constant rates of heating and the master sintering curves approaches and calculating the diffusion coefficients by exploiting the results of the sintering runs enabled to propose that densification was probably controlled by grain boundary diffusion and grain growth by the grain boundaries. An activation energy around 525 kJ/mol was obtained for densification, which was close to what was reported for grain boundary diffusion of plutonium cations in U_{0.55}Pu_{0.45}O_{2-x} polycrystalline materials. The sintered microstructure appeared homogeneous regarding the plutonium and uranium cations spatial distribution. By combining the master sintering curve approach for anisothermal and isothermal conditions, it was possible to predict the evolution of the relative density over time for any type of thermal path.

Keywords: Sintering; oxides; microstructure; MOX

The submitted paper is original and has not been or is not being submitted to the peer review process to any other journal

*Corresponding author: guillaume.bernard-granger@cea.fr

1. Introduction

1 Mixed OXides (MOX, $\text{UO}_2\text{-PuO}_2$) nuclear fuels are used in light water
2 reactors and are also candidates for fast neutron ones. The advantage of such
3
4 fuels is that it allows the use of plutonium oxide recovered from the recycling
5
6 of spent UOX (Uranium OXide) fuels, as well as depleted uranium oxide
7
8 resulting from the UOX fuel enrichment protocol.
9

10
11
12 The MOX fuel takes usually the shape of cylindrical pellets (typically 10 mm
13
14 of diameter and height) that are industrially manufactured using a powder
15
16 metallurgy dry-route process. In a first step, the UO_2 and PuO_2 raw powders
17
18 are dry ground/milled together. Then the pellets are shaped using automatic
19
20 uniaxial pressing and sintered at high temperature under a specific atmosphere
21
22 by controlling the oxygen partial pressure. Depending on the application, the
23
24 sintered pellets may also encounter an additional rectification step of their
25
26 lateral surface by dry centerless-grinding. Then, they are introduced into tubes
27
28 made from an appropriate material, referred to as the cladding. These tubes
29
30 are sealed and loaded onto an assembly, with specific configurations, that will
31
32 be positioned in the core of a given nuclear reactor.
33
34
35
36
37

38 The Pu content incorporated in a MOX fuel formulation depends on the type
39
40 of reactor where it will be **burned**. For light water nuclear reactors, the
41
42 Pu/(U+Pu) ratio typically ranges between 3 and 11 mol%. For fast neutron
43
44 nuclear reactors it is not clearly specified **up to now**, but it should **range**
45
46 between 15 and 35 mol% **[1-2]**. If the “oxygen over metal” ratio, named O/M,
47
48 is 2.00 for MOX fuels devoted to light water nuclear reactors, it should be
49
50 strictly comprised between 2.00 and 1.94 for the ones dedicated to fast neutron
51
52 nuclear reactors mainly to avoid pellets/cladding interaction and to be able to
53
54 control the thermal conductivity of the fuel at high temperature. Therefore,
55
56 MOX fuels dedicated to fast neutron nuclear reactors are sintered under more
57
58 reducing conditions than those for light water nuclear reactors.
59
60
61
62
63
64
65

1 Sintering at high temperatures of MOX fuels has been investigated in the past
2 regarding the plutonium oxide content incorporated and in different kinds of
3 atmospheres (oxidizing, inert and reducing) [1-5]. Despite experiments
4 perfectly well conducted, the results were not conclusive in identifying the
5 mechanisms controlling densification and development of the microstructure.
6
7

8
9
10
11 In comparison to the traditional powder-metallurgy process, the
12 freeze-granulation route has been shown to be an advantageous approach to
13 manufacture MOX fuel pellets [6]. Highly flowable, dustless and easy-to-press
14 MOX granules were elaborated using such a process [6]. Then, the purpose of
15 this paper is to rigorously investigate the sintering behavior in reducing
16 conditions of powder compacts made of such granules.
17
18
19
20
21
22
23
24
25

26 **2. Experimental procedure**

27 *2.1. Freeze granulated powder*

28
29 A $\text{UO}_2\text{-PuO}_2$ powder, containing 15 mol% Pu/(U+Pu), was prepared using the
30 freeze-granulation protocol defined by La Lumia [6]. The UO_2 powder used
31 was synthesized through a dry route by reduction of UF_6 in gas phase. It
32 contains also 8.5 wt% of the U_3O_8 phase and has an overall O/M ratio of 2.20.
33
34 The PuO_2 powder was obtained by oxalic precipitation of plutonium (IV)
35 nitrate and calcination in air. Its O/M ratio is 2.00. More details about both
36 powders are available in the literature [7]. Fig. 1 shows the morphology of
37 some individual granules observed using scanning electron microscopy (SEM,
38 Supra 55 VP, Zeiss). They have a spherical shape and are devoid of any central
39 cavity. Laser particle size distribution measured in dry mode (Mastersizer
40 3000, Malvern Panalytical, Mie configuration, compressed air pressure in the
41 venturi fixed to 0.1 bar) is also shown in Fig. 1. The most important point is
42 that the median diameter for the number distribution ($[D_n(50)]$) is around 100
43 μm and that there are no granules smaller than 30 μm . The Pu/(U+Pu) content
44 in the freeze-granulated powder was determined to be 14.4(\pm 0.4) mol% using
45
46
47
48
49
50
51
52
53
54
55
56
57
58
59
60
61
62
63
64
65

thermal ionization mass spectrometry (TIMS, VG-54 magnetic sector mass spectrometer, Isotopx).

2.2. Calculation of the theoretical density for sintering

The target O/M ratio after sintering is around 1.96 which is representative of MOX fuel for fast neutron reactors. Philipponneau proposed a relationship linking the lattice parameter, a , to the Pu/(U+Pu) molar content, y , and the deviation from stoichiometry, x , for $U_{1-y}Pu_yO_{2-x}$ solid solutions [8]:

$$a(pm) = 547 - 7.4y + 32x \quad (1)$$

Assuming that the Pu content will not vary during sintering and neglecting the americium content present in the freeze-granulated powder (the β decay of the small content of ^{241}Pu present in the PuO_2 raw powder gives rise to an amount of ^{241}Am estimated to be 1.84 mol% $Am/(Pu+Am)$), a lattice parameter of 547.21 pm is then calculated for the $U_{0.856}Pu_{0.144}O_{1.960}$ composition. Because $U_{1-y}Pu_yO_{2-x}$ solid solutions have a fluorite structure (Fm $\bar{3}m$, space group 225), the theoretical density at room temperature is then given by:

$$\rho_0^{th} = \frac{4(M_{U/Pu} + 1.96M_O)}{N_A a^3} \quad (2)$$

where $M_{U/Pu}$ is the molar mass of U/Pu, M_O is the molar mass of O, N_A is the number of Avogadro and a is the lattice parameter. The UO_2 and PuO_2 raw powders used are mainly constituted by ^{238}U and ^{239}Pu isotopes, respectively. Assuming a molar mass of 238 g for U/Pu, a value around 11.0 g/cm³ is then calculated for ρ_0^{th} .

We are aware that the starting UO_2 powder contains 8.5 wt% of U_3O_8 that transforms into $UO_{2.00}$ in a reducing atmosphere above 600 °C [9]. This contribution was not taken into account in the calculation of the theoretical

1 density at room temperature as U_3O_8 reduction occurs before any significant
2 sintering. The O/M ratio of the sample is also supposed to change continuously
3 during the sintering experiments under reducing conditions [10]: i) between
4 300 and 900 °C the reduction of UO_{2+x} into $UO_{2.00}$ proceeds, ii) in the range
5 900-1700 °C the reduction of PuO_2 or $U_{1-y}Pu_yO_2$ solid solution formed at high
6 temperature into PuO_{2-x} or $U_{1-y}Pu_yO_{2-x}$ takes place. However, we decided to
7 keep 11.0 g/cm³ as the theoretical density for the duration of each experiment
8 (temperature between 20 and 1700 °C) because the impact on the theoretical
9 density value would be marginal.

20 2.3. Green compacts

21 Cylindrical samples (diameter of 5.4 mm and a height around 7 mm) were
22 obtained by uniaxial pressing the freeze-granulated powder with a compaction
23 pressure of 450 MPa (manual hydraulic press, Atlas 25, Specac). The
24 geometric relative green density was around 57(± 0.4)% for all the different
25 compacts prepared.

34 It has to be emphasized that all samples underwent a debinding thermal
35 treatment before sintering to remove the organic compounds (dispersant and
36 binder) which were incorporated during the preparation of the freeze-
37 granulated powder [6]. Thus, samples were exposed at 600 °C for 2h in an
38 Ar/4 vol% H₂ atmosphere humidified with 1200 vpm of water (oxygen partial
39 pressure and oxygen potential set to 1.3×10^{-27} bar and -450 kJ/mol at 600 °C,
40 respectively).

50 2.4. Sintering

51 Kato proposed the following expression for the O/M ratio of $U_{1-y}Pu_yO_{2+x}$ MOX
52 formulations taking into account the thermal and atmosphere conditions they
53 are submitted to [11]:
54
55
56
57

$$\frac{O}{M}$$

$$\begin{aligned}
 &= 2 \\
 &- \left\{ \left[e^{\frac{44.0+55.8y}{R}} \times e^{-\frac{376000}{RT}} \times p_{O_2}^{-\frac{1}{2}} \right]^{-5} \right. \\
 &+ \left[\left(e^{\frac{68.8+131.3y}{R}} \times e^{-\frac{515000}{RT}} \right)^{\frac{1}{2}} \times p_{O_2}^{-\frac{1}{4}} \right]^{-5} \\
 &+ \left[\left(2 \times e^{\frac{153.5-96.5y+331.0y^2}{R}} \times e^{-\frac{891000}{RT}} \right)^{\frac{1}{3}} \times p_{O_2}^{-\frac{1}{3}} \right]^{-5} \\
 &\left. + \left(\frac{1}{2}y \right)^{-5} \right\}^{\frac{1}{5}} + \left\{ e^{\frac{-22.8-84.5y}{R}} \times e^{-\frac{105000}{RT}} \times p_{O_2}^{\frac{1}{2}} \right\} \quad (3)
 \end{aligned}$$

where y is, as before, the Pu/(U+Pu) molar content, p_{O_2} is the oxygen partial pressure of the atmosphere, R is the universal gas constant and T the absolute temperature. The oxygen partial pressure is related to the oxygen potential $\overline{\Delta G_{O_2}}$ by the well-known expression:

$$\overline{\Delta G_{O_2}} = RT \ln \left(\frac{p_{O_2}}{p_{O_2}^*} \right) \quad (4)$$

where $p_{O_2}^*$ is the unit of the oxygen partial pressure (1 bar).

The green pellets were sintered from room temperature to 1700 °C in a high temperature dilatometer (DIL402C, Setaram) under Ar/4 vol% H₂. According to Kato, the oxygen partial pressure required to obtain a O/M ratio around 1.96 for a MOX **composition** containing 14.4 mol% Pu/(U+Pu), at 1700 °C, is around 4.1×10^{-13} bar, which gives an oxygen potential of -468 kJ/mol. Accordingly, the atmosphere was monitored and controlled with an oxygen pump (Gen'air, Setnag) in order to have a constant water concentration of 100 vpm (calculated using the Wheeler approach [12] to obtain the target oxygen partial pressure and oxygen potential at 1700 °C) during the sintering runs.

1 Heating rates fixed to 2, 3 and 4 °C/min were used for the sintering runs. The
 2
 3
 4 isothermal duration was ranging from 0 to 4h and the target temperature from
 5
 6 1600 to 1700 °C (for the only test completed at 1600 °C, the oxygen partial
 7
 8 pressure and the oxygen potential were adjusted regarding equations (3) and
 9
 10 (4) to obtain a O/M ratio around 1.96). The equipment contribution was
 11
 12 subtracted based on a blank measurement made with an Al₂O₃ reference
 13
 14 sample for each experiment.
 15

16
 17
 18 Because the mass of the samples does not change significantly between the
 19
 20 debinded and fired states (maximum weight loss of 1% resulting from
 21
 22 reduction of the oxide-based material), the following relation is obtained [13-
 23
 24 14]:
 25

$$26$$

$$27$$

$$28$$

$$29$$

$$30$$

$$31$$

$$32$$

$$33$$

$$34$$

$$35$$

$$36$$

$$37$$

$$38$$

$$39$$

$$40$$

$$41$$

$$42$$

$$43$$

$$44$$

$$45$$

$$46$$

$$47$$

$$48$$

$$49$$

$$50$$

$$51$$

$$52$$

$$53$$

$$54$$

$$55$$

$$56$$

$$57$$

$$58$$

$$59$$

$$60$$

$$61$$

$$62$$

$$63$$

$$64$$

$$65$$

$$D_{(T)}(\%) = D_0 \frac{1}{\xi^2 \left[1 + \frac{\Delta L_{(T)}}{L_0} \right]^3} e^{3\alpha(T-T_0)} \quad (5)$$

where: $D_{(T)}$ is defined as the sample instantaneous relative density, D_0 is the
 relative green density, ξ is representative of the shrinkage anisotropy of the
 sample and is given by $\xi = \frac{\phi_f L_0}{\phi_0 L_f} = \frac{\phi_{(T)} L_0}{\phi_0 L_{(T)}}$ with ϕ_f the final diameter, L_f the
 final height, ϕ_0 the initial diameter, L_0 the initial height, $\phi_{(T)}$ the instantaneous
 diameter and $L_{(T)}$ the instantaneous height, $\Delta L_{(T)} = L_{(T)} - L_0$ (<0) is the
 sample height variation, α is the linear thermal expansion coefficient, T is the
 instantaneous absolute temperature and T_0 the absolute room temperature.
 From a practical point of view, α is determined from the cooling steps of the
 dilatometer runs. An average value of $11.6(\pm 0.6) \times 10^{-6}$ is retained. All the
 sintering tests carried out have shown that the parameter ξ is very close to 1.

1 The density of the sintered samples was measured using the Archimedes
2 method with bromobenzene (dry, immersed and humid weights, three series of
3 measurements were carried out for each sample).
4
5
6

7 2.4. Grain size measurement

8 For green compacts, the grain size is determined from a fracture surface
9 observed using SEM (Supra 55 VP, Zeiss) in secondary electron mode. For
10 sintered samples, each complete sample is embedded in a resin and a mirror
11 longitudinal polished cross section is prepared including a final
12 mechanical-polishing step using 250 and 40 nm colloidal silica suspensions
13 that reveals sufficiently the grain boundaries of the polycrystal using the
14 backscattered electron mode during SEM (Mira 3, Tescan) observations. Then,
15 for both kinds of samples, it is easy to determine the average grain size by the
16 intercept method (at least 300 grains are taken into account, correction factor
17 set to 1.56) from SEM images [15].
18
19
20
21
22
23
24
25
26
27
28
29
30
31

32 2.4. Plutonium distribution in the sintered samples

33 The longitudinal polished cross sections of some sintered samples were
34 characterized using electron probe microanalysis (EPMA, SX100, Cameca).
35 Measurements performed at 20 kV at the U-M α and Pu-M β lines allowed the
36 U-Pu distribution to be assessed. The Pu content in the mappings was
37 estimated based on quantitative measurements along 500 μ m lines obtained by
38 applying the ZAF method and using UO $_2$ and PuO $_2$ samples as standards for
39 U, Pu and O.
40
41
42
43
44
45
46
47
48
49
50

51 **3. Results and discussion**

52 Fig. 2a shows the variation of the relative density as a function of temperature
53 for the different heating rates. Whatever the heating rate, samples start to
54 densify around 600 °C. The lower the heating rate, the higher the relative
55 density for a given temperature. Such a behavior is not new and was
56
57
58
59
60
61
62
63
64
65

1 previously reported for numerous non-radioactive oxides [13-14, 16-17]. Sato
2 argued that the lower the heating rate, the longer the exposure time and the
3 higher the shrinkage and relative density reached at a given temperature [16].
4
5
6

7 Fig. 2b shows how the instantaneous densification rate is changing as a
8 function of temperature for the three heating rates retained. The higher the
9 heating rate, the higher the instantaneous densification rate whatever the
10 temperature. This trend was also previously reported for non-radioactive
11 oxides [13-14, 18]. More interesting is the fact that the curves do not exhibit
12 the traditional bell-shape with a clear maximum densification rate. If it might
13 seem that a maximum densification rate around $5.7 \times 10^{-5} \text{ s}^{-1}$ is positioned at
14 1680 °C when the heating rate is fixed to 2 °C/min, no maximum of the
15 densification rate does appear for the two other heating rate values. This type
16 of sample requires a significant residence time at high temperature to reach
17 high densities under the atmospheric conditions applied. The temperature rise
18 phase alone does not allow materials with closed porosity to be obtained (Fig.
19 2a). Similar trends have been reported by Kutty [3] in the past and more
20 recently by Nakamichi [5].
21
22
23
24
25
26
27
28
29
30
31
32
33
34
35
36
37

38 Fig. 2c is a zoom of Fig. 2b in the 600-1200 °C temperature range. Whatever
39 the heating rate, the densification rate exhibits a maximum value around 775
40 °C. It signifies that densification starts around 600 °C and slows-down from
41 775 °C. Similar results were reported by several authors investigating the
42 sintering behavior in different kinds of atmospheres of UO₂-20 wt% PuO₂ [3],
43 UO₂-30 wt% PuO₂ [19] fuels and UO₂-30 wt% CeO₂ surrogates [20].
44 According to them, the densification slow-down is correlated with the onset of
45 a UO₂-PuO₂ or UO₂-CeO₂ solid solution formation. Even if additional
46 experiments are required (X-ray diffraction experiments at high temperature
47 will be completed in the future), we postulate that a solid solution forms in the
48 densifying samples around 775 °C, whatever the heating rate used. Because
49
50
51
52
53
54
55
56
57
58
59
60
61
62
63
64
65

1 the solid solution is formed by the interdiffusion of Pu^{4+} cations into the UO_2
2 lattice and U^{4+} cations into the PuO_2 lattice it decreases the densification rate
3 until completion and then densification restarts with a polycrystalline sample
4 made of $\text{U}_{1-y}\text{Pu}_y\text{O}_{2-x}$ grains. Accordingly, when densification resumes around
5 1000°C, the samples are more homogeneous and can be described as a
6 polycrystalline body constituted by pores and grains of $\text{U}_{1-y}\text{Pu}_y\text{O}_{2-x}$ solid
7 solutions, rather than UO_2 and PuO_2 grains alone.
8
9
10
11
12
13
14
15

16 Fig. 2d shows the variation of the absolute instantaneous densification rate in
17 function of $D(T)$ for the different heating rates retained. The three curves
18 overlap meaning that the densification mechanism is independent of the
19 heating rate used.
20
21
22
23
24
25

26 Fig. 3 shows examples of the green and sintered microstructures observed
27 using SEM (sample relative density increases from left to right for each row of
28 micrographs). When observed in two dimensions and as soon as densification
29 proceeds, the residual pores becomes isolated, switching from a vermicular
30 morphology to a more rounded shape. For all sintered samples, the elemental
31 grains constituting the polycrystalline material are well faceted with an
32 equilibrium shape.
33
34
35
36
37
38
39
40
41

42 Fig. 4 shows results from EPMA observations concerning the plutonium
43 spatial distribution and its quantification in sintered samples having relative
44 densities between 84.2 and 97.9%. The Pu repartition inside all pellets is
45 homogenous, notably compared to samples manufactured by conventional
46 powder metallurgy processes [21-22]. However, small and local enrichments,
47 with Pu contents between 40-60 mol%, are still visible. MOX fuels with a very
48 homogeneous U/Pu distribution are thought to have a better behavior under
49 irradiation in reactors by limiting/preventing the formation of the typical high
50 burnup structure [23-24].
51
52
53
54
55
56
57
58
59
60
61
62
63
64
65

1
2
3
4
5
6
7
8
9
10
11
12
13
14
15
16
17
18
19
20
21
22
23
24
25
26
27
28
29
30
31
32
33
34
35
36
37
38
39
40
41
42
43
44
45
46
47
48
49
50
51
52
53
54
55
56
57
58
59
60
61
62
63
64
65

Knowing the relative density and the grain size of each sample (green and sintered ones), it is possible to construct the “grain size versus relative density” trajectory named the “sintering path”, as shown on Fig. 5. The experimental points seem to belong to a single trajectory (dashed curve, first level fitting using the Lab Fit Curve Fitting Software) that is independent of sintering temperature, soak time and heating rate. Accordingly, the grain size can be described as a monotonous function of the relative density. A multitude of sintering experimental conditions led to the same microstructure, as was previously reported for other non-radioactive oxides [13-14, 18].

The experimental points constituting the sintering path shown on Fig. 5 were fitted with theoretical expressions linking the grain size to the relative density [25]. The best agreement coefficient value amongst these fits, almost 1, is obtained when grain growth is controlled by the grain boundaries and densification is controlled by grain boundary diffusion (see the fit on Fig. 6a). Nonetheless, other mechanism combinations are leading to determination coefficient values above 0.99. At this point, we must remain careful regarding the mechanisms controlling densification and grain growth.

Let us now focus on the determination of the apparent activation energy for the mechanism controlling densification. The equation for the densification rate can be separated into temperature-dependent, grain size-dependent and density-dependent quantities as follows [14, 17, 26]:

$$\frac{dD}{dt} = A \frac{F[D]}{G^n} e^{-\frac{Q_d}{RT}} \quad (6)$$

where A is a constant, $F[D]$ is a function only of density, Q_d is the apparent activation energy for the mechanism controlling densification, R is the universal gas constant, T is the instantaneous absolute temperature, G is the

1 grain size, n is the grain size exponent whose value depends on whether the
 2 densification rate is controlled by lattice diffusion ($n = 3$) or grain-boundary
 3 diffusion ($n = 4$).
 4
 5
 6
 7

8 The instantaneous densification rate may be also written as:
 9

$$10 \frac{dD}{dt} = \frac{dD}{dT} \frac{dT}{dt} \quad (7)$$

11
 12
 13
 14
 15
 16
 17 where dT/dt , the heating rate, is held constant during anisothermal sintering
 18 experiments and is named ζ . By combining relations (6), (7) and rearranging,
 19
 20
 21 the following expression is obtained:
 22
 23
 24

$$25 \ln \left[T \frac{dD}{dT} \frac{dT}{dt} \right] = -\frac{Q_d}{RT} + \ln\{F[D]\} + \ln(A) - n\ln(G) \quad (8)$$

26
 27
 28
 29
 30 A plot of the left-hand side of relation (8) versus $1/T$ would give a value for
 31 Q_d provided that the data points are taken at a constant value of D and G . Fig.
 32
 33
 34 **5** shows that each value of relative density corresponds to a single value of
 35 grain size, whatever the sintering conditions. Points for a constant value of D
 36
 37
 38
 39 are then generated by changing the heating rate. The measurements led to
 40
 41
 42 values of Q_d at different values of D . This formalism is known as the CRH
 43
 44
 45 method (Constant Rates of Heating). Using this approach leads to an almost
 46
 47
 48 constant apparent activation energy of 528 ± 7 kJ/mol for the mechanism
 49
 50
 51 controlling densification, as shown on Fig. 6b.

52
 53
 54 A second method to determine the apparent activation energy for the
 55
 56
 57 mechanism controlling densification is to construct the Master Sintering Curve
 58
 59
 60 (MSC). By extending the analysis of sintering beyond the confined segments
 61
 62
 63 described by the individual stage models, it was shown for an isotropic
 64
 65 shrinkage (true for the freeze-granulated powder investigated here because the

value of ξ in relation (1) is very close to 1) and if there exists only one dominant diffusion mechanism (either volume or grain boundary diffusion), that the densification rate may be expressed as [27-29]:

$$\frac{dD}{Dt} = \frac{3\gamma_{sv}\Omega\Gamma[D]\Phi_0}{RT(G[D])^n} e^{-\frac{Q_d}{RT}} \quad (9)$$

where γ_{sv} is the solid/vapor surface tension, $\Phi_0 = \Phi_{v0}$ and $n = 3$ for volume diffusion, $\Phi_0 = \delta b\Phi_{b0}$ with δ_b the grain boundary thickness and $n = 4$ for grain boundary diffusion (Φ_0 is the pre-exponential factor of the diffusion coefficient), $\Gamma[D]$ and $G[D]$ (the grain size) are functions only of the relative density, T_0 is the temperature at which densification is effectively starting (assumed to be 1000 °C, at the end of solid solution formation) and the other parameters were described previously. Equation (9) is similar to Equation (6) and also to densification rate expressions established in the past for a control by volume or grain boundary diffusion when sintering fine-grained ceramics [25]. Su obtained the well-known relationship after rearranging and integrating expression (9) [28-29]:

$$\frac{R}{3\gamma_{sv}\Omega\Phi_0} \int_{D_0}^D \frac{(G[D])^n}{D\Gamma[D]} dD = \int_0^t \frac{e^{-\frac{Q_d}{RT}}}{T} dt \quad (10)$$

Stating $\Theta_d(h/K) = \int_0^t \frac{e^{-\frac{Q_d}{RT}}}{T} dt$ gives:

$$\frac{R}{3\gamma_{sv}\Omega\Phi_0} \int_{D_0}^D \frac{(G[D])^n}{D\Gamma[D]} dD = \int_0^t \frac{e^{-\frac{Q_d}{RT}}}{T} dt = \Theta_d(h/K) = \frac{1}{\zeta} \int_{T_0}^T \frac{e^{-\frac{Q_d}{RT}}}{T} dT \quad (11)$$

Because the left-hand site of Equation (11) is a function only of relative density, the MSC is defined as the relationship between relative density D and Θ_d [28-29]. To construct the MSC curve under anisothermal sintering

1 conditions, we used the results from the dilatometer runs, the trapezoidal
2 approximation and a curve-fitting procedure to determine the value of Q_d by
3 minimizing the residual sum of squares (RSS) between the experimental and
4 calculated values, assuming that all points must line up to form a single curve.
5 Such an analysis leads to the results shown in Figs. 6c and 6d. The apparent
6 activation energy for the mechanism controlling densification is then
7 calculated to be around 510 ± 10 kJ/mol (the uncertainty is only estimated).
8
9
10
11
12
13
14
15

16 Thereby, an apparent average activation energy of 525 ± 9 kJ/mol, associated
17 with the densification mechanism, is determined from the CRH and MSC
18 methods (average value and standard deviation calculated by taking into
19 account the four values obtained from the CRH method and the single value
20 calculated from the MSC analysis).
21
22
23
24
25
26
27

28 By expanding the concept of the MSC approach to isothermal sintering
29 conditions (use of the same value of activation energy as that previously
30 determined under anisothermal conditions), it is possible to predict the
31 evolution of the instantaneous relative density as a function of temperature for
32 any thermal cycle including anisothermal and isothermal steps. The results
33 obtained are visible in Figure 7 where calculated (Calc) cycles are compared to
34 experimental (Exp) ones. The agreement between the calculated and
35 experimental values is very good. The use of such an approach makes it
36 possible to design an ideal sintering cycle from the point of view of its speed
37 (the cooling step is not taken into account because it depends on the type of
38 furnace used) and its consumption of resources while making it possible to
39 achieve a final relative density greater than 95% (MOX fuel criterion for the
40 fast neutron reactors).
41
42
43
44
45
46
47
48
49
50
51
52
53
54
55
56

57 Now let's try to specify in more detail what could be the densification
58 mechanism involved. Noyau measured the volume and grain boundary
59
60
61
62
63
64
65

diffusion coefficients of plutonium cations in an $U_{0.55}Pu_{0.45}O_{2-x}$ polycrystalline material, for an oxygen potential set to -395 kJ/mol [30]. He obtained:

$$D_v^{Pu} = 11.02 \times 10^{-4} e^{-\frac{625000}{RT}} m^2/s \quad (12)$$

$$D_b^{Pu} = 4.51 \times 10^{-2} e^{-\frac{506000}{RT}} m^2/s \quad (13)$$

where D_v^{Pu} and D_b^{Pu} are the volume and grain boundary diffusion coefficients.

The activation energy for the grain boundary diffusion of plutonium cations obtained by Noyau (around 506 kJ/mol), is very close to the one (525 kJ/mol) that was determined from the CRH and MSC methods for densification of the freeze-granulated powder investigated in the study reported in this paper.

Let us now calculate the grain boundary diffusion coefficient involved in densification by exploiting the sintering experiments completed on the freeze-granulated powder and by considering the theoretical expression for the densification rate.

When densification is controlled by grain boundary diffusion, the densification rate in the secondary and tertiary stages of sintering is given by [25]:

$$\frac{dD}{dt} = \frac{400\Omega\gamma_{sv}\delta_b D_b}{RTG^4} \quad (14)$$

which turns to:

$$D_b = \frac{RTG^4}{400\Omega\gamma_{sv}\delta_b} \frac{dD}{dt} \quad (15)$$

By using a typical value of 1 nm for δ_b and 1 J/m² for γ_{sv} , the grain boundary diffusion coefficient variation in function of temperature was calculated from the sintering experiment conducted on the freeze-granulated powder with a

1 heating rate fixed to 2 °C/min, between 1100 and 1680 °C (at 1100 °C, the
 2 sample relative density is 57.4% against 84.6% at 1680 °C). Then it was
 3 compared to the experimental values obtained by Noyau. The results are
 4 summarized on Fig. 8. As implicitly introduced into relation (9), the grain
 5 boundary diffusion coefficient can also be expressed as:
 6
 7
 8
 9

$$10 \quad D_b = \Phi_{0b} e^{-\frac{Q}{RT}} \quad (16)$$

11 with Φ_{0b} the pre-exponential factor and Q the activation energy of the grain
 12 boundary diffusion mechanism. For each data series, Φ_{0b} and Q values are
 13 also given in Fig. 8.
 14
 15

16 For temperatures higher than 1525 °C, corresponding to a relative density
 17 above 69.2%, the experimental values of the grain boundary diffusion
 18 coefficient of plutonium cations in a polycrystalline $U_{0.55}Pu_{0.45}O_{2-x}$ material are
 19 very close to the ones calculated from the sintering run completed on the
 20 freeze-granulated powder. In the same time, the activation energy calculated
 21 from the sintering experiment is 494 kJ/mol, which is similar to 506 kJ/mol
 22 obtained by Noyau. For temperatures below 1525 °C and for relative density
 23 values below 69.2%, the calculated values of the grain boundary diffusion
 24 coefficient from the sintering experiment are now much higher than the
 25 experimental values obtained by Noyau. More than that, the activation energy
 26 values differ a lot: 506 kJ/mol for Noyau against 180 kJ/mol from the sintering
 27 run completed on the freeze-granulated powder.
 28
 29
 30
 31
 32
 33
 34
 35
 36
 37
 38
 39
 40
 41
 42
 43
 44
 45
 46
 47
 48
 49
 50

51 Accordingly, for temperatures above 1525 °C (relative density above 69.2%),
 52 densification of the freeze granulated powder is most probably controlled by
 53 the grain boundary diffusion of plutonium cations. In the same time, it is also
 54 likely that grain growth is controlled by grain boundaries (best fit of theoretical
 55 expressions, result shown on Fig. 6a). For temperatures lower than 1525 °C
 56
 57
 58
 59
 60
 61
 62
 63
 64
 65

(relative density below 69.2%) another mechanism may control densification. Such a possible change was not identified using the CRH and MSC approaches. More experimental results are then needed to conclude regarding this point.

In the future, transmission electron microscopy observations will be completed on some of the sintered samples. Particular attention will be paid to the analysis of grain boundaries (nature, defects, chemical segregation...), to the identification of a possible space charge zone in their vicinity and to the potential variation of chemical composition when moving from a grain boundary to the core of the surrounding grains.

Additional sintering runs will be also completed on freeze-granulated powders incorporating 25 and 33 mol% Pu/(U+Pu) and the results will be compared to the ones reported in this paper.

4. Conclusions

Sintering investigations on a $\text{UO}_2\text{-PuO}_2$ freeze-granulated powder containing 15 mol% Pu/(U+Pu) were completed under reducing conditions (oxygen potential set to -468 kJ/mol at 1700 °C) for a target O/M ratio of 1.96. After formation of a $\text{U}_{1-y}\text{Pu}_y\text{O}_{2\pm x}$ solid solution that ended around 1000 °C, the sintered microstructure appeared homogeneous regarding the plutonium and uranium cations spatial distribution. Depending on the sintering parameters, the final sintered relative density achieved was well above 95%.

By constructing the “grain size versus relative density” trajectory named the “sintering path”, using the CRH and MSC approaches and calculating the grain boundary diffusion coefficient from the sintering runs, it appeared that densification was most probably controlled by the grain boundary diffusion of plutonium cations and grain growth by the grain boundaries at temperatures

1 above 1525 °C. For temperatures below 1525 °C, different mechanisms may
2 be possibly involved.
3

4
5 By combining the master sintering curve approach for anisothermal and
6 isothermal conditions, it was possible to predict the evolution of the relative
7 density over time for any type of thermal path (heating rate, sintering soak
8 temperature and holding time).
9

10
11
12
13 **Acknowledgements:** The authors warmly thank Gauthier Jouan, Romain
14 Lauwerier, Jean-Robert Sevilla, Romain Vauchy and Patrice Signoret for their
15 precious help during the experiments carried out within the framework of this
16 study.
17
18
19
20
21
22
23
24
25
26
27
28
29
30
31
32
33
34
35
36
37
38
39
40
41
42
43
44
45
46
47
48
49
50
51
52
53
54
55
56
57
58
59
60
61
62
63
64
65

References

- 1
2
3
4 [1] S. Noyau, F. Audubert, P.M. Martin, A. Maitre. Influence of the oxygen
5 potential on the sintering of UO_2 -45% PuO_2 . J. Eur. Ceram. Soc. 35 (2011)
6 3651-3663. <https://doi.org/10.1016/j.jeurceramsoc.2015.05.006>
7
8
9
10
11
12 [2] S. Berzati, S. Vaudez, R.C. Belin, J. L  chelle, Y. Marc, J.C. Richaud, J.M.
13 Heintz. Controlling the oxygen potential to improve the densification and the
14 solid solution formation of uranium-plutonium mixed oxides. J. Nucl. Mater.
15 447 (2014) 115-124. <https://doi.org/10.1016/j.jnucmat.2013.12.014>
16
17
18
19
20
21
22 [3] T.R.G. Kutty, P.V. Hegde, K.B. Khan, S. Majumdar, D.S.C. Purushotham.
23 Sintering studies on UO_2 - PuO_2 pellets with varying PuO_2 content using
24 dilatometry. J. Nucl. Mater. 282 (2000) 54-65. [https://doi.org/10.1016/S0022-](https://doi.org/10.1016/S0022-3115(00)00394-9)
25
26
27
28
29
30
31
32 [4] T.R.G. Kutty, P.V. Hegde, R. Keswani, K.B. Khan, S. Majumdar, D.S.C.
33 Purushotham. Densification behaviour of UO_2 -50% PuO_2 pellets by
34 dilatometry. J. Nucl. Mater 264 (1999) 10-19. [https://doi.org/10.1016/S0022-](https://doi.org/10.1016/S0022-3115(98)00490-5)
35
36
37
38
39
40
41
42 [5] S. Nakamichi, S. Hirooka, M. Kato, T. Sunaoshi, A. T. Nelson, K. J.
43 McClellan. Effect of O/M ratio on sintering behavior of $(\text{Pu}_{0.3}\text{U}_{0.7})\text{O}_{2-x}$. J.
44 Nucl. Mater. 535 (2020) 152188.
45
46
47
48
49
50
51
52 [6] F. La Lumia, L. Ramond, C. Pagnoux, P. Coste, F. Lebreton, J.R. Sevilla,
53 G. Bernard-Granger. Dense and homogeneous MOX fuel pellets manufactured
54 using the freeze granulation route. J. Amer. Ceram. Soc. 103 (2020) 3020-
55
56
57
58
59
60
61
62
63
64
65

1 [7] F. La Lumia, L. Ramond, C. Pagnoux, G. Bernard-Granger. Preparation
2 and co-dispersion of TiO₂-Y₂O₃ suspensions through the study of their
3 rheological and electrokinetic properties. *Ceram. Int.* 45 (2019) 3023-3032.
4
5
6
7
8 <https://doi.org/10.1016/j.ceramint.2018.10.123>
9

10
11 [8] R. Vauchy, A.C. Robisson, R.C. Belin, P.M. Martin, A.C. Scheinost, F.
12 Hodaj. Room temperature oxidation of hypostoichiometric uranium-plutonium
13 mixed oxides U_{1-y}Pu_yO_{2-x}. A depth-selective approach. *J. Nucl. Mater.* 465
14 (2015) 349-357. <https://doi.org/10.1016/j.jnucmat.2015.05.033>
15
16
17
18
19

20
21 [9] F. Valdivieso, M. Pijolat, M. Soustelle, J. Jourde. Reduction of uranium
22 oxide U₃O₈ into uranium dioxide UO₂ by ammonia. *Proceedings of the XIVth*
23 *International Symposium on the Reactivity of Solids, Budapest*, pp. 117-122,
24 2000
25
26
27
28
29

30
31 [10] S. Vaudez, J. Léchelle, S. Berzati, J.M. Heintz. Assessing the oxygen
32 stoichiometry during the sintering of (U, Pu)O₂ fuel. *J. Nucl. Mater.* 460
33 (2015) 221-225. <https://doi.org/10.1016/j.jnucmat.2015.02.005>
34
35
36
37
38

39
40 [11] M. Kato, M. Watanabe, T. Matsumoto, S. Hirooka, M. Akashi. Oxygen
41 potentials, oxygen diffusion coefficients and defect equilibria of
42 nonstoichiometric of (U, Pu)O_{2±x}. *J. Nucl. Mater.* 487 (2017) 424-432.
43
44
45
46
47 <https://doi.org/10.1016/j.jnucmat.2017.01.056>
48
49

50
51 [12] V. J. Wheeler, I.G. Jones. Thermodynamic and composition changes in
52 UO_{2±x} (x < 0.005) at 1950 K. *J. Nucl. Mater.* 42 (1972) 117-121.
53
54
55 [https://doi.org/10.1016/0022-3115\(72\)90018-9](https://doi.org/10.1016/0022-3115(72)90018-9)
56
57
58
59
60
61
62
63
64
65

1 [13] G. Bernard-Granger, C. Guizard. Apparent activation energy for the
2 densification of a commercially available granulated zirconia powder. J. Amer.
3 Ceram. Soc. 90 (2007) 1246-1250. [https://doi.org/10.1111/j.1551-](https://doi.org/10.1111/j.1551-2916.2006.01415.x)
4 [2916.2006.01415.x](https://doi.org/10.1111/j.1551-2916.2006.01415.x)
5
6

7
8
9 [14] N. Benameur, G. Bernard-Granger, A. Addad, S. Raffy, C. Guizard.
10 Sintering analysis of a fine-grained alumina – magnesia spinel powder. J.
11 Amer. Ceram. Soc. 94 (2011) 1388-1396. [https://doi.org/10.1111/j.1551-](https://doi.org/10.1111/j.1551-2916.2010.04271.x)
12 [2916.2010.04271.x](https://doi.org/10.1111/j.1551-2916.2010.04271.x)
13
14
15
16

17
18
19 [15] M.I. Mendleson. Average grain size in polycrystalline ceramics. J. Amer.
20 Ceram. Soc. 52 (1969) 443-446. [https://doi.org/10.1111/j.1151-](https://doi.org/10.1111/j.1151-2916.1969.tb11975.x)
21 [2916.1969.tb11975.x](https://doi.org/10.1111/j.1151-2916.1969.tb11975.x)
22
23
24
25

26
27 [16] E. Sato, C.P. Carry. Yttria doping and sintering of submicrometer-grained
28 α -alumina. J. Amer. Ceram. Soc. 79 (1996) 2156-2160.
29 <https://doi.org/10.1111/j.1151-2916.1996.tb08950.x>
30
31
32
33
34

35
36 [17] J. Wang, R. Raj. Estimate of the activation energies for boundary
37 diffusion from rate-controlled sintering of pure alumina and alumina doped
38 with zirconia or titania. J. Amer. Ceram. Soc. 73 (1990) 1172-75.
39 <https://doi.org/10.1111/j.1151-2916.1990.tb05175.x>
40
41
42
43
44

45
46 [18] G. Bernard-Granger, C. Guizard, A. Addad. Sintering of an ultra pure α -
47 alumina powder: I. Densification, grain growth and sintering path. J. Mater.
48 Sci. 42 (2007) 6316-6324. <https://doi.org/10.1007/s10853-006-1206-1>
49
50
51
52
53

54 [19] R. Manzel, W.D. Dorr. Fabrication of $\text{UO}_2\text{-Gd}_2\text{O}_3$ fuel pellets. Ceram.
55 Bull. 59 (1980) 601-616
56
57
58
59
60
61
62
63
64
65

1 [20] W. Dorr, S. Hellmann, G. Mages. Study of the formation of $\text{UO}_2\text{-PuO}_2$
2 solid solution by means of $\text{UO}_2\text{-CeO}_2$ simulate. J. Nucl. Mater. 140 (1986) 7-
3 10. [https://doi.org/10.1016/0022-3115\(86\)90190-X](https://doi.org/10.1016/0022-3115(86)90190-X)
4
5

6
7 [21] T. Gervais, D. Favet, L. Paret, S. Vaudez. (U, Pu) O_{2-x} MOX pellet for
8 Astrid reactor project. Proceedings of the International Conference on Fast
9 Reactors and Related Fuel Cycles: Next Generation Nuclear Systems for
10 Sustainable Developments, Yekaterinburg, 2017
11
12
13
14
15

16
17 [22] G. Oudinet, I. Munoz-Viallard, L. Aufore, M.J. Gotta, J.M. Becker, G.
18 Chiarelli, R.Castelli. Characterization of plutonium distribution in MIMAS
19 MOX by image analysis. J. Nucl. Mat. 375 (2008) 86-94.
20
21
22
23
24
25
26
27
28
29
30
31
32
33
34
35
36
37
38
39
40
41
42
43
44
45
46
47
48
49
50
51
52
53
54
55
56
57
58
59
60
61
62
63
64
65

[23] J. Noirot, L. Desgranges, J. Lamontagne. Detailed characterizations of
high-burnup structures in oxide fuels. J. Nucl. Mater. 372 (2008) 318-339.
<https://doi.org/10.1016/j.jnucmat.2007.04.037>

[24]. J. Noirot, Y. Pontillon, J. Lamontagne, I. Zacharie-Aubrun, K. Hanifi, P.
Bienvenu, L. Desgranges. High burn-up structure in nuclear fuel: impact on
fuel behavior. EPJ Web of Conferences 115 (2016) 04005

[25] G. Bernard-Granger, C. Guizard. New relationships between relative
density and grain size during solid-state sintering of ceramic powders. Acta
Mater. 56 (2008) 6273–6282. <https://doi.org/10.1016/j.actamat.2008.08.054>

[26] J. Wang, R. Raj. Activation energy for the sintering of two-phase
alumina-zirconia ceramics. J. Am. Ceram. Soc.74 (1991) 1959–63.
<https://doi.org/10.1111/j.1151-2916.1991.tb07815.x>

1 [27] J.D. Hansen, R.P. Rusin, M.H. Teng, D.L. Johnson. Combined-stage
2 sintering model. J. Am. Ceram. Soc. 75 (1992) 1129–35.
3 <https://doi.org/10.1111/j.1151-2916.1992.tb05549.x>
4
5

6
7 [28] H. Su, D.L. Johnson. Master sintering curve: a practical approach to
8 sintering. J. Am. Ceram. Soc. 79 (1996) 3211–7.
9 <https://doi.org/10.1111/j.1151-2916.1996.tb08097.x>
10
11

12 [29] D.L. Johnson. Finding and utilizing the master sintering curve.
13 Proceedings of Sintering 03: International conference on the science,
14 technology and application of sintering, Penn State University, 2003
15
16

17 [30] S. Noyau. Etude des phénomènes d'autodiffusion et d'interdiffusion du
18 plutonium dans les céramiques de type $U_{1-y}Pu_yO_{2\pm x}$. PhD Thesis, University of
19 Limoges, 2012
20
21
22
23
24
25
26
27
28
29
30
31
32
33
34
35
36
37
38
39
40
41
42
43
44
45
46
47
48
49
50
51
52
53
54
55
56
57
58
59
60
61
62
63
64
65

Figure captions

1
2
3
4 Fig. 1: a) SEM micrograph of granules constituting the freeze-granulated
5 powder; b) and c) SEM micrographs of the inside of an individual granule; d)
6 and e) U and Pu EDS mapping (arbitrary color scale) of the inside of an
7 individual granule (same area as that shown on c); f) Volume/number
8 distributions from laser granulometer tests in dry mode on the freeze-
9 granulated powder.

10
11
12
13
14
15
16
17
18 Fig. 2: a) Relative density in function of temperature; b) Densification rate in
19 function of temperature; c) Zoom of b) in the 600-1200 °C temperature range;
20 d) Absolute densification rate in function of temperature. Three different
21 heating rates values have been used: 2 °C/min (solid blue line), 3 °C/min
22 (dashed red line) and 4 °C/min (dashed green line).

23
24
25
26
27
28
29
30 Fig. 3: Microstructure of a green sample and different sintered samples. For
31 each sintered microstructure are given in order of appearance the heating rate
32 value, the sintering temperature, the time spend at the sintering temperature,
33 the relative density D and the grain size G of the sintered sample.

34
35
36
37
38
39
40 Fig. 4: Sintering path. Plot of the grain size as a function of relative density.
41 For each experimental point, the values given are the heating rate, the sintering
42 temperature and the time spent at the sintering temperature.

43
44
45
46
47
48 Fig. 5: Colored pseudo-quantified Pu mapping by EPMA on different sintered
49 samples having a relative density ranging from 84.2 to 97.9%. For each map
50 are given in order of appearance the heating rate value, the sintering
51 temperature, the time spend at the sintering temperature, the relative density D
52 and the grain size G of the sintered sample.

1
2
3
4
5
6
7
8
9
10
11
12
13
14
15
16
17
18
19
20
21
22
23
24
25
26
27
28
29
30
31
32
33
34
35
36
37
38
39
40
41
42
43
44
45
46
47
48
49
50
51
52
53
54
55
56
57
58
59
60
61
62
63
64
65

Fig. 6: a) Fitting of the experimental points for a scenario based on densification being controlled by grain boundary diffusion and grain growth by the grain boundaries; b) Determination of the apparent activation energy for densification using the anisothermal CRH method. Different relative density values have been fixed for the three heating rates applied during the sintering tests; c) Determination of the apparent activation energy for densification using the anisothermal MSC method – Residual sum of squares (RSS), d) Determination of the apparent activation energy for densification using the anisothermal MSC method – MSC curve.

Fig. 7: Extension of the concept of the MSC approach to predict the evolution of the instantaneous relative density as a function of temperature for any thermal cycle including anisothermal and isothermal steps. Calculated values are compared to experimental ones.

Fig. 8: Calculation of the grain boundary diffusion coefficient from sintering experiments. Comparison to the experimental values obtained by Noyau for a $U_{0.55}Pu_{0.45}O_{2-x}$ polycrystalline material [30]. The pre-exponential Φ_{0b} and activation energy Q values are indicated

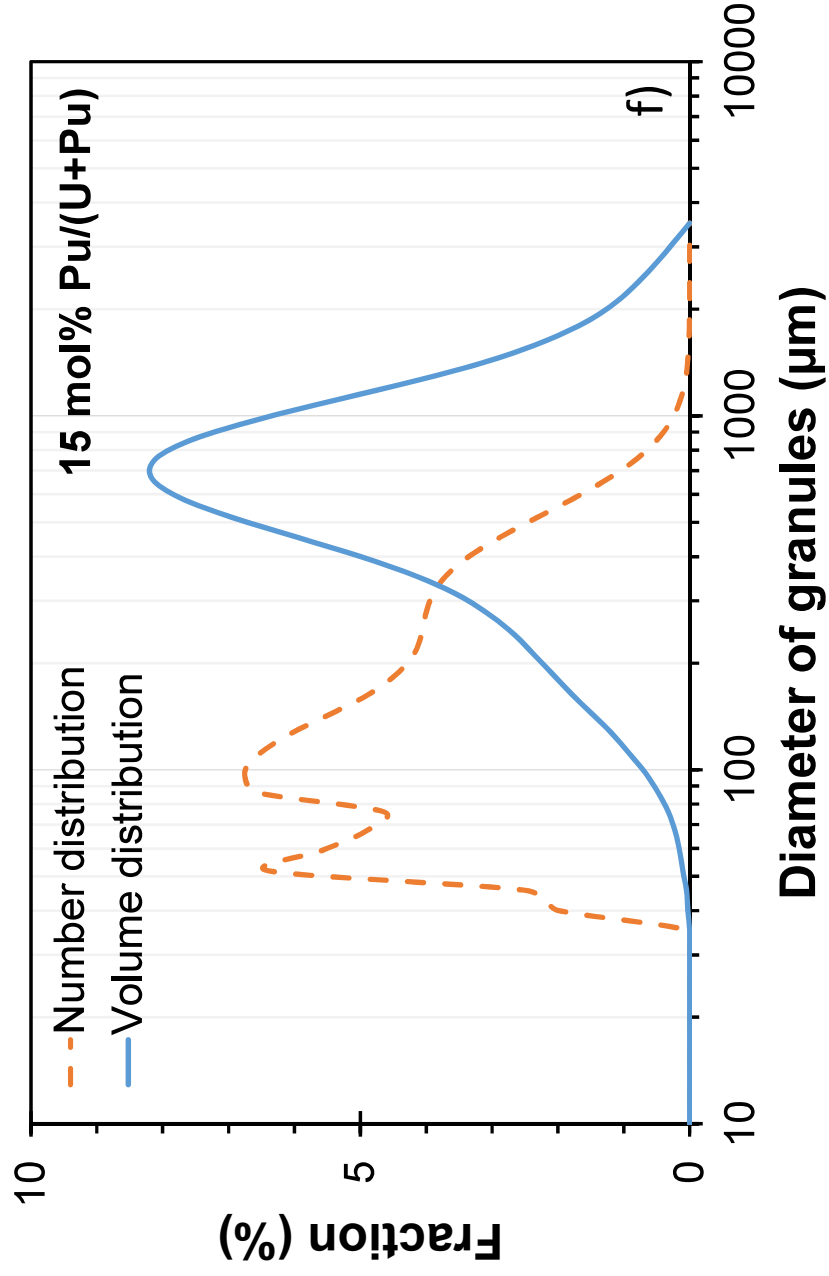
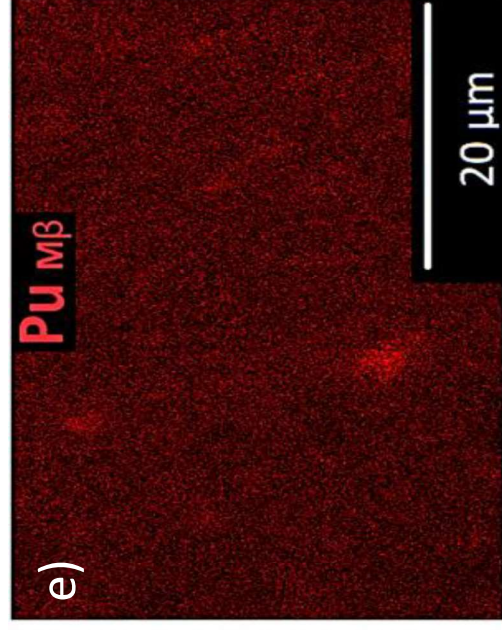
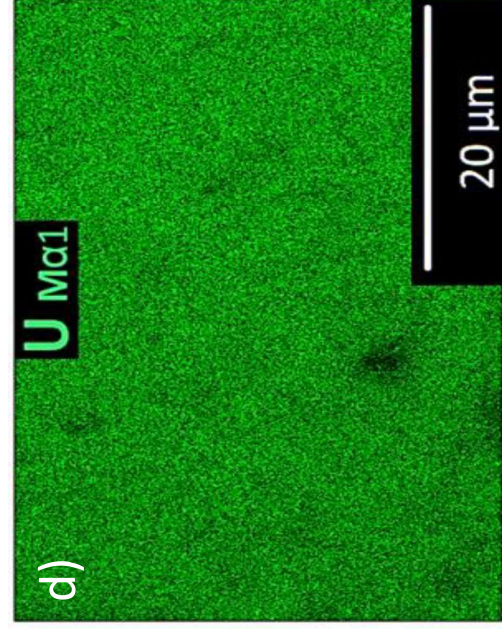
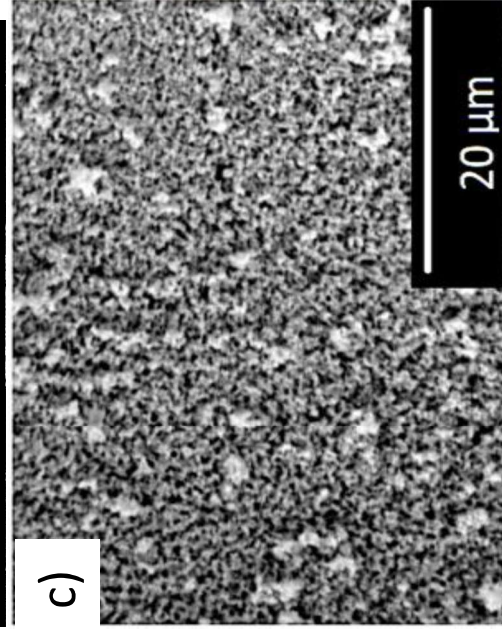
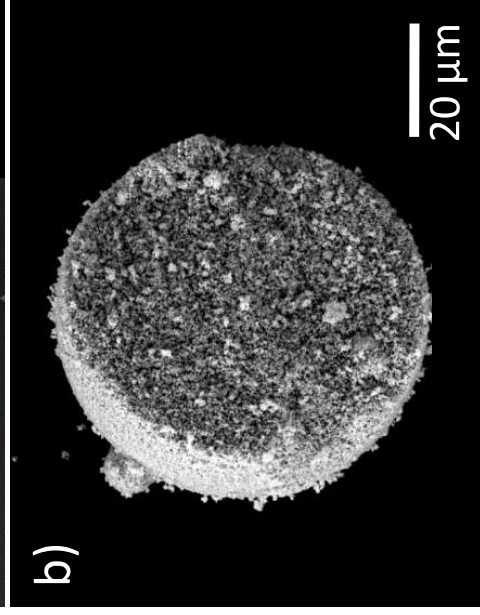
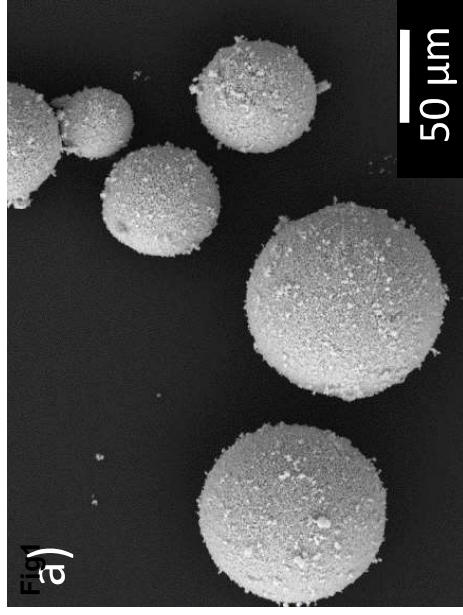


Fig2

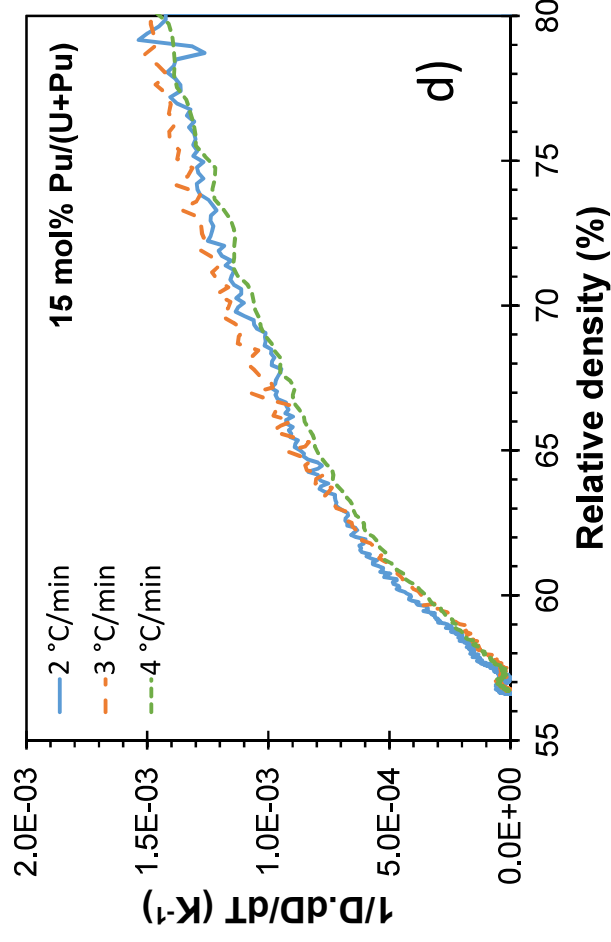
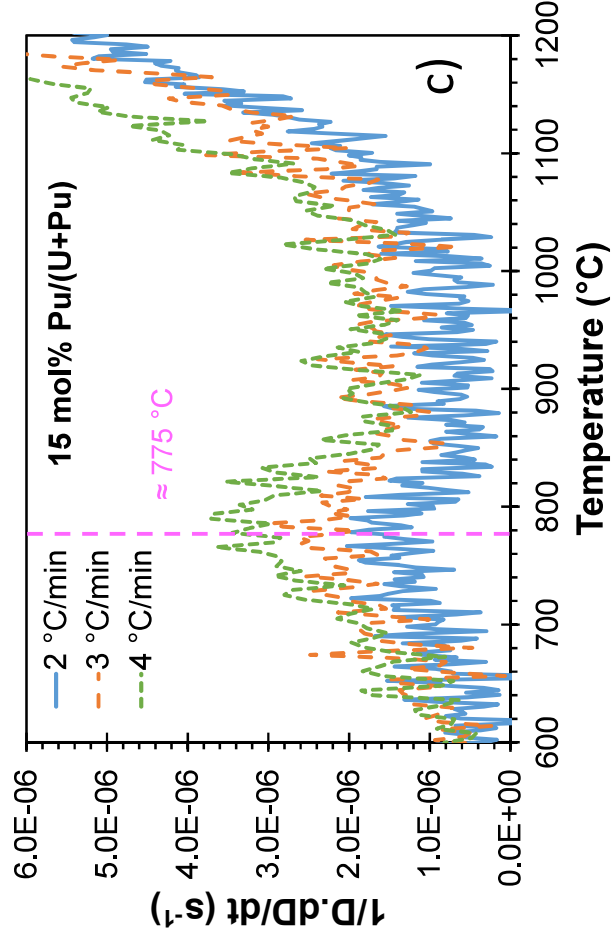
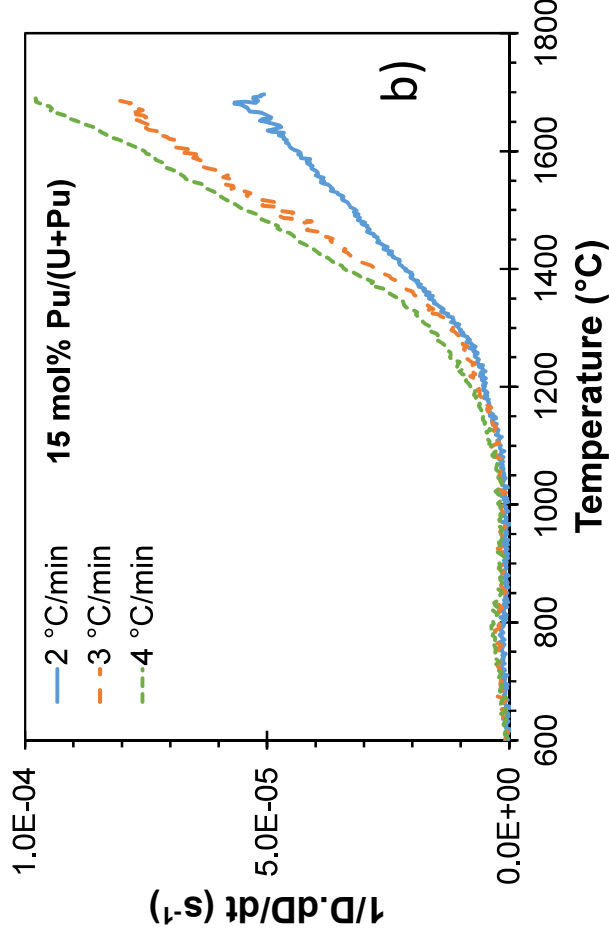
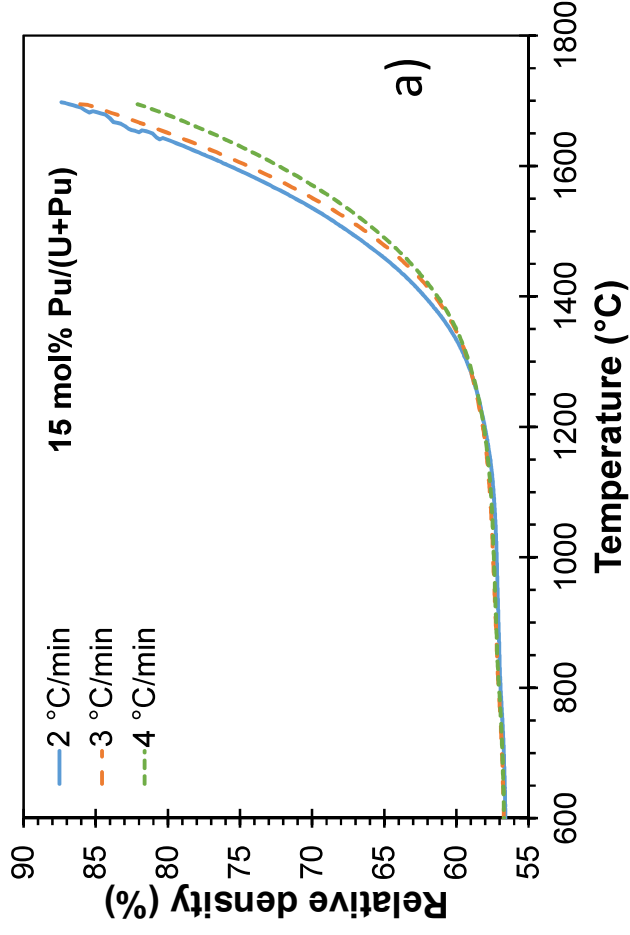


Fig3

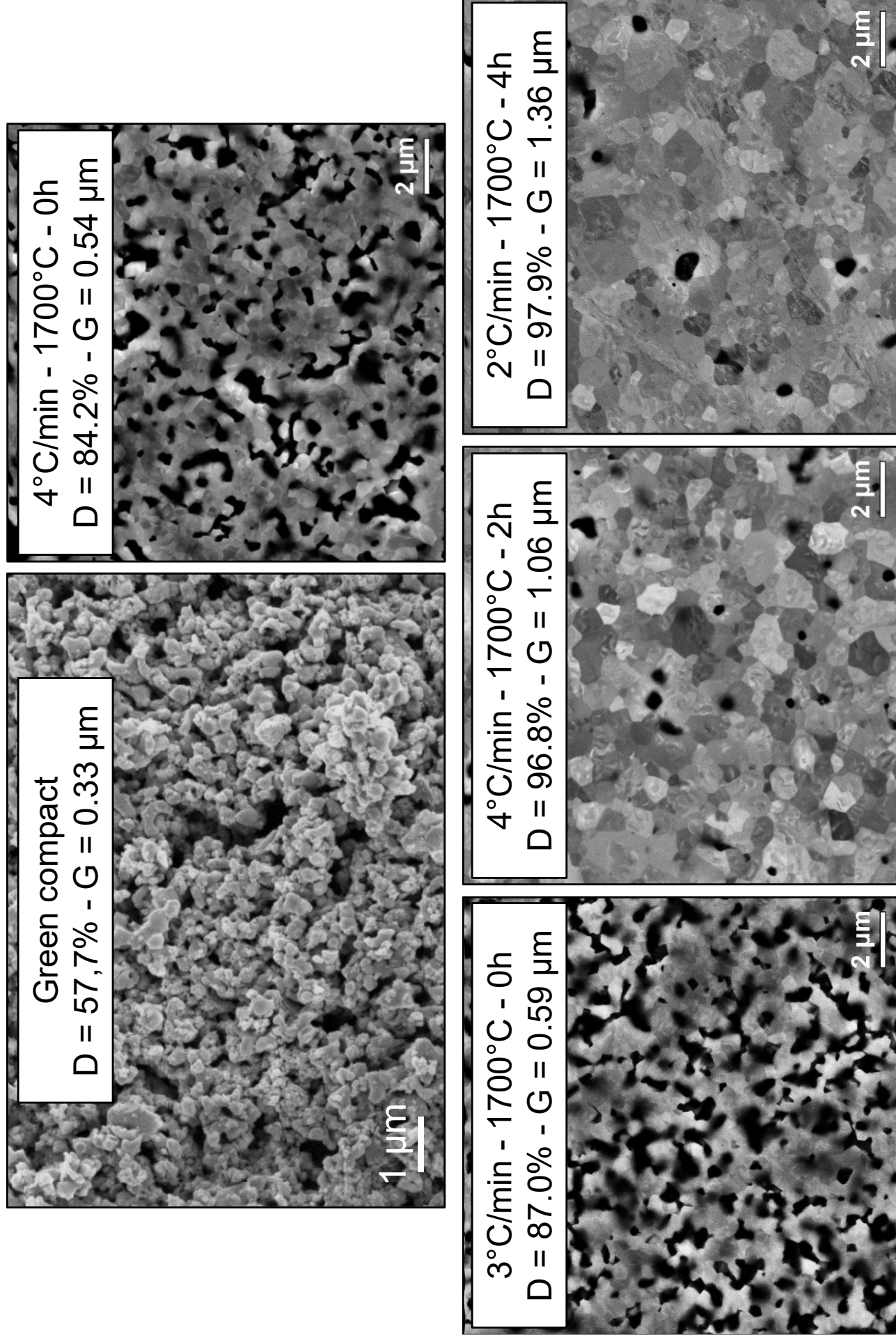


Fig4

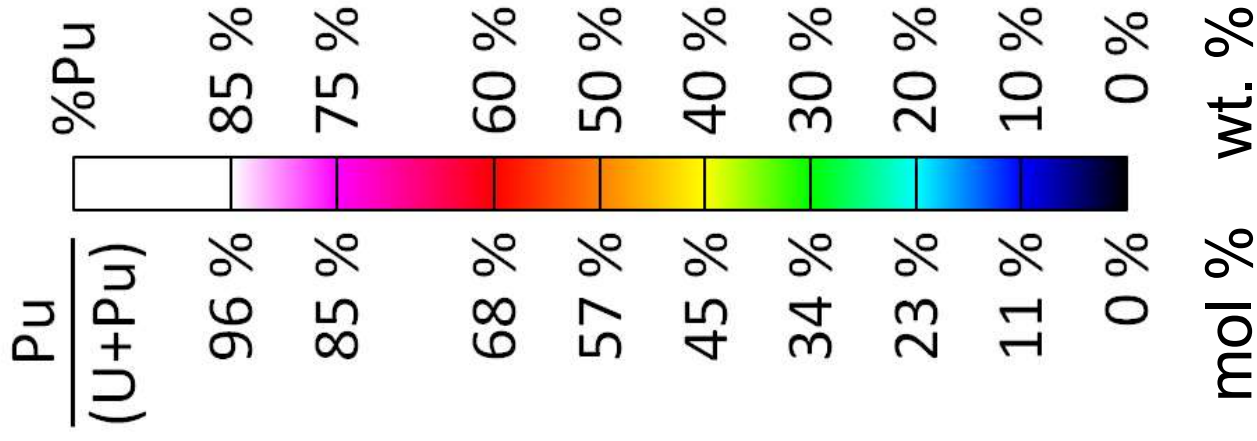
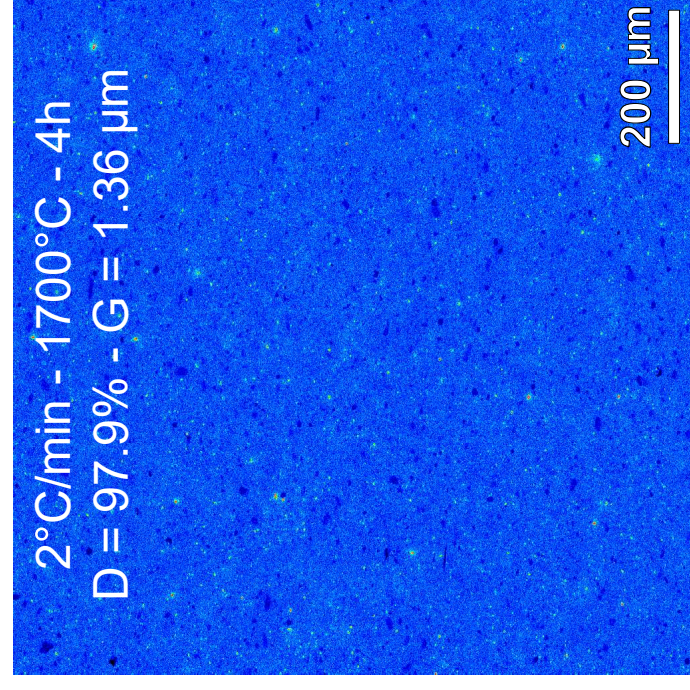
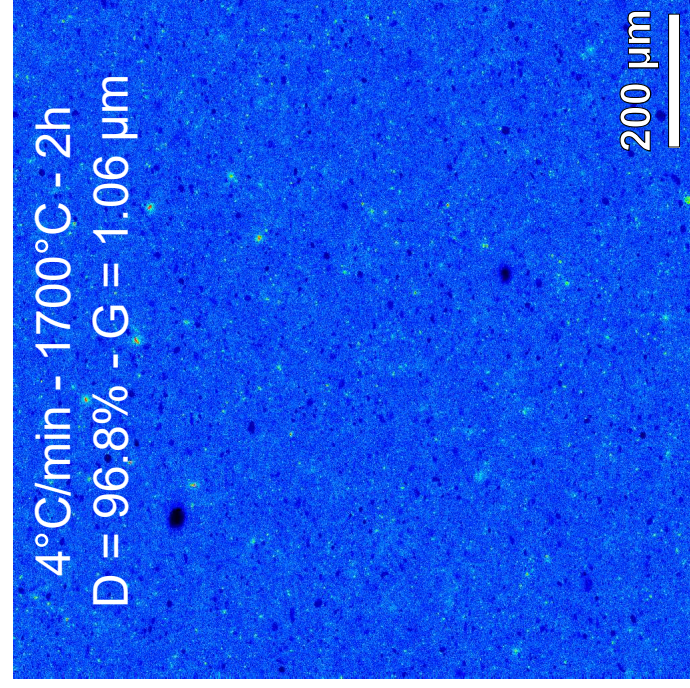
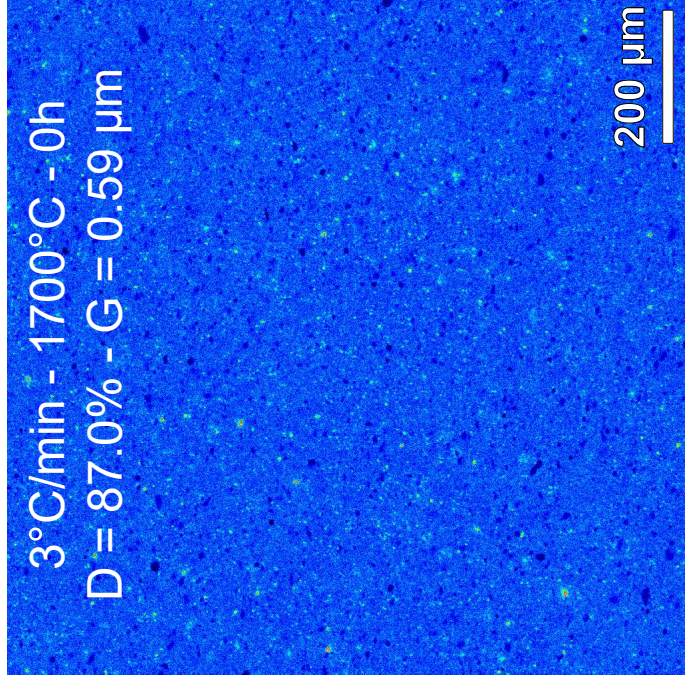
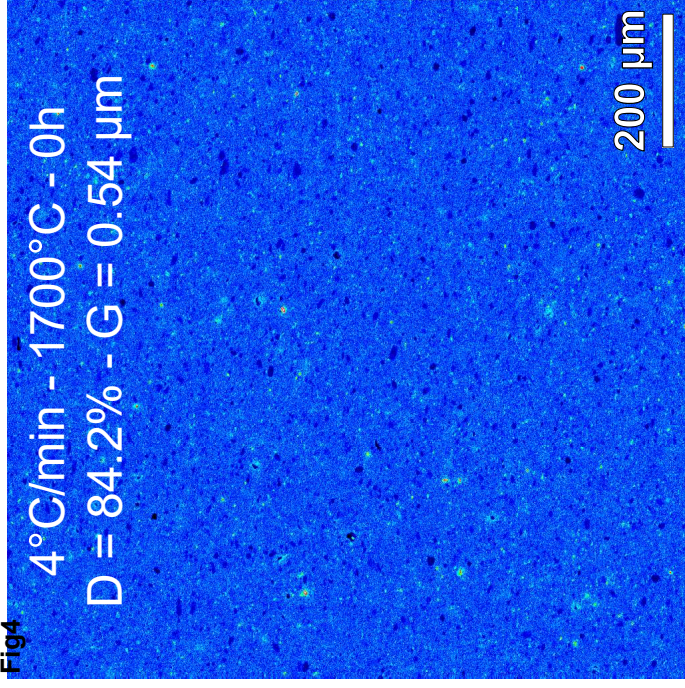


Fig5

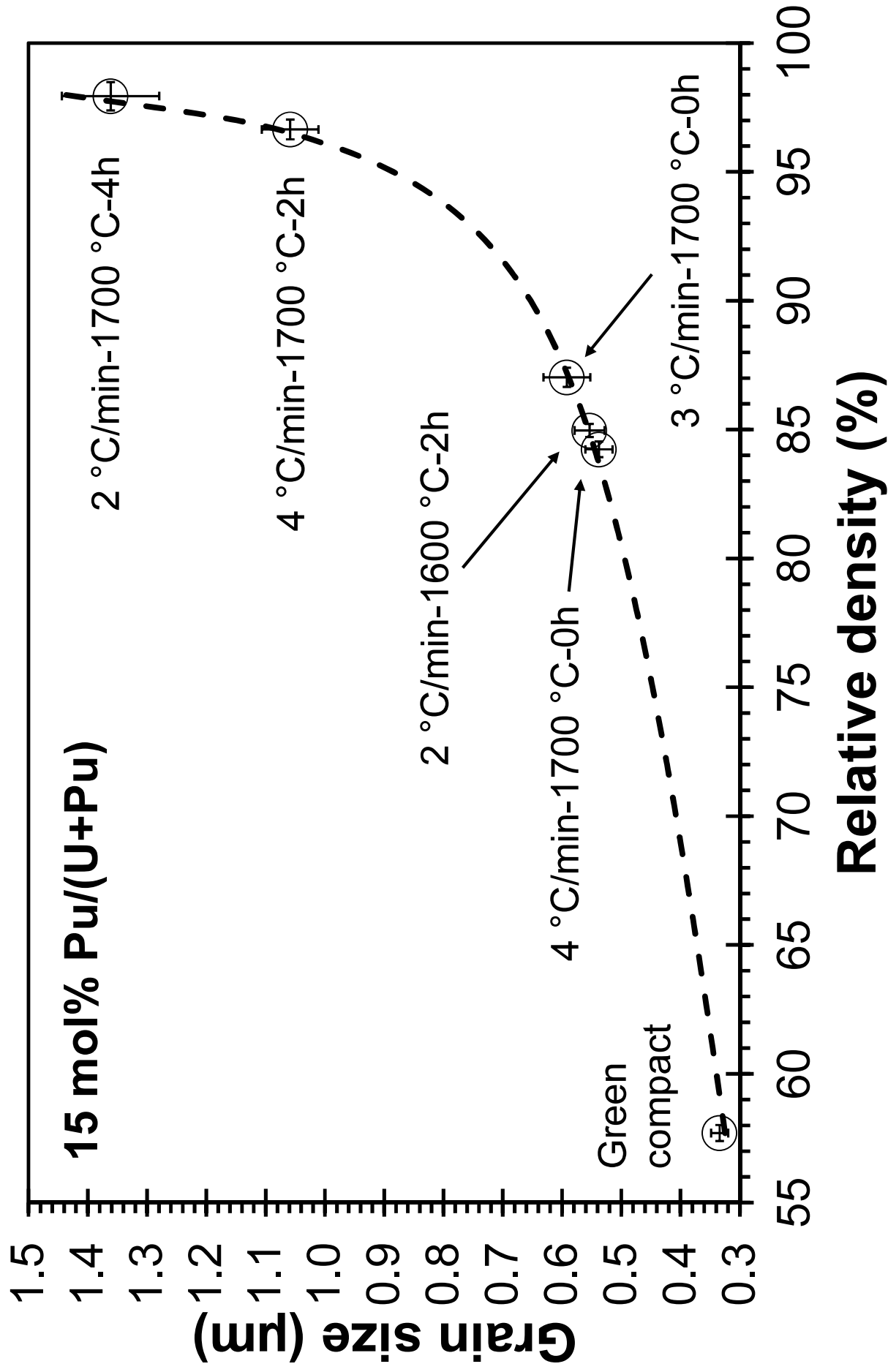


Fig6

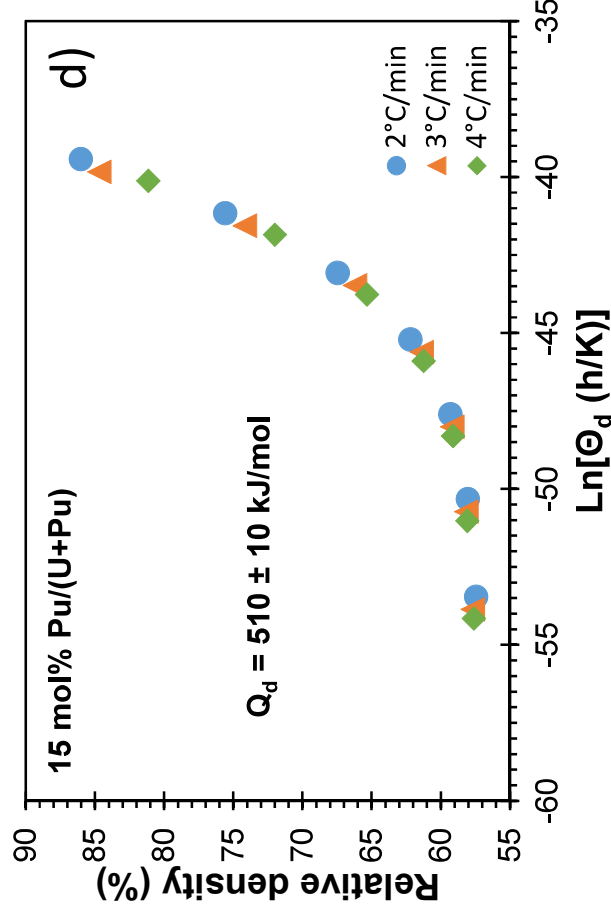
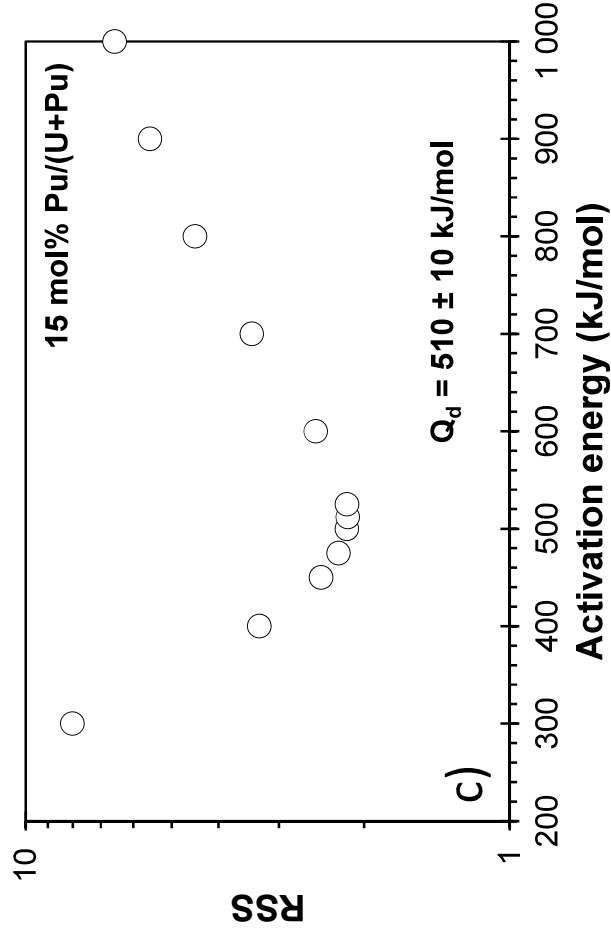
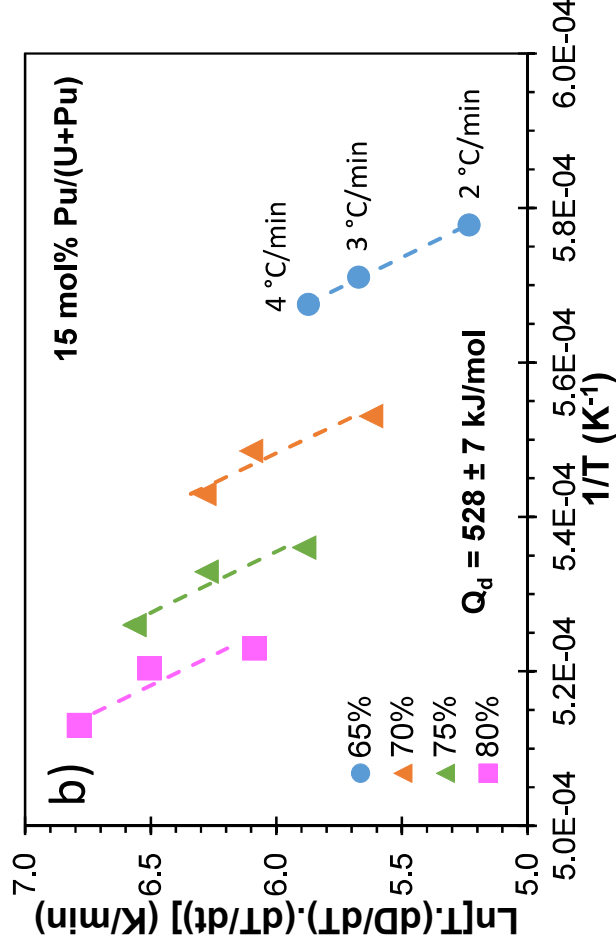
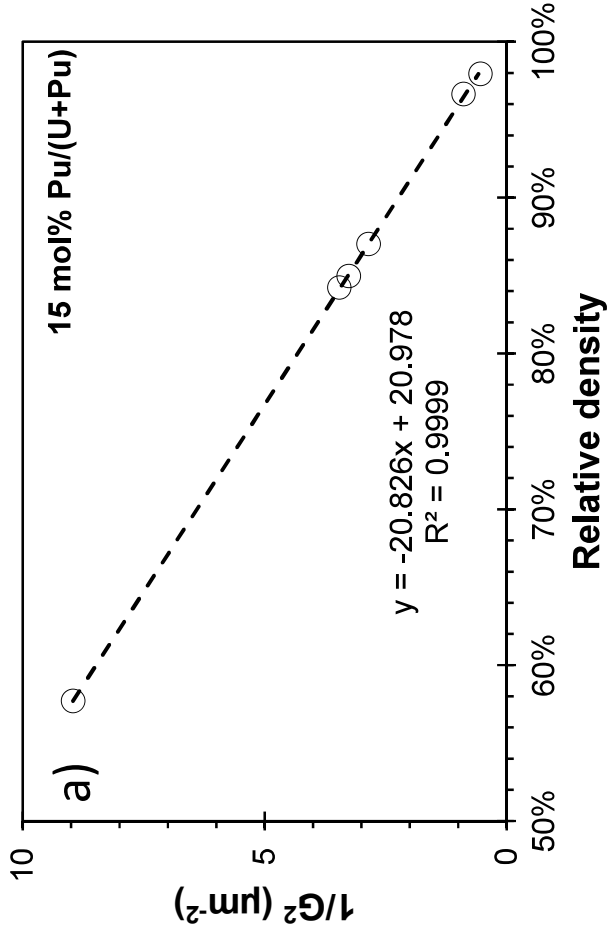


Fig7

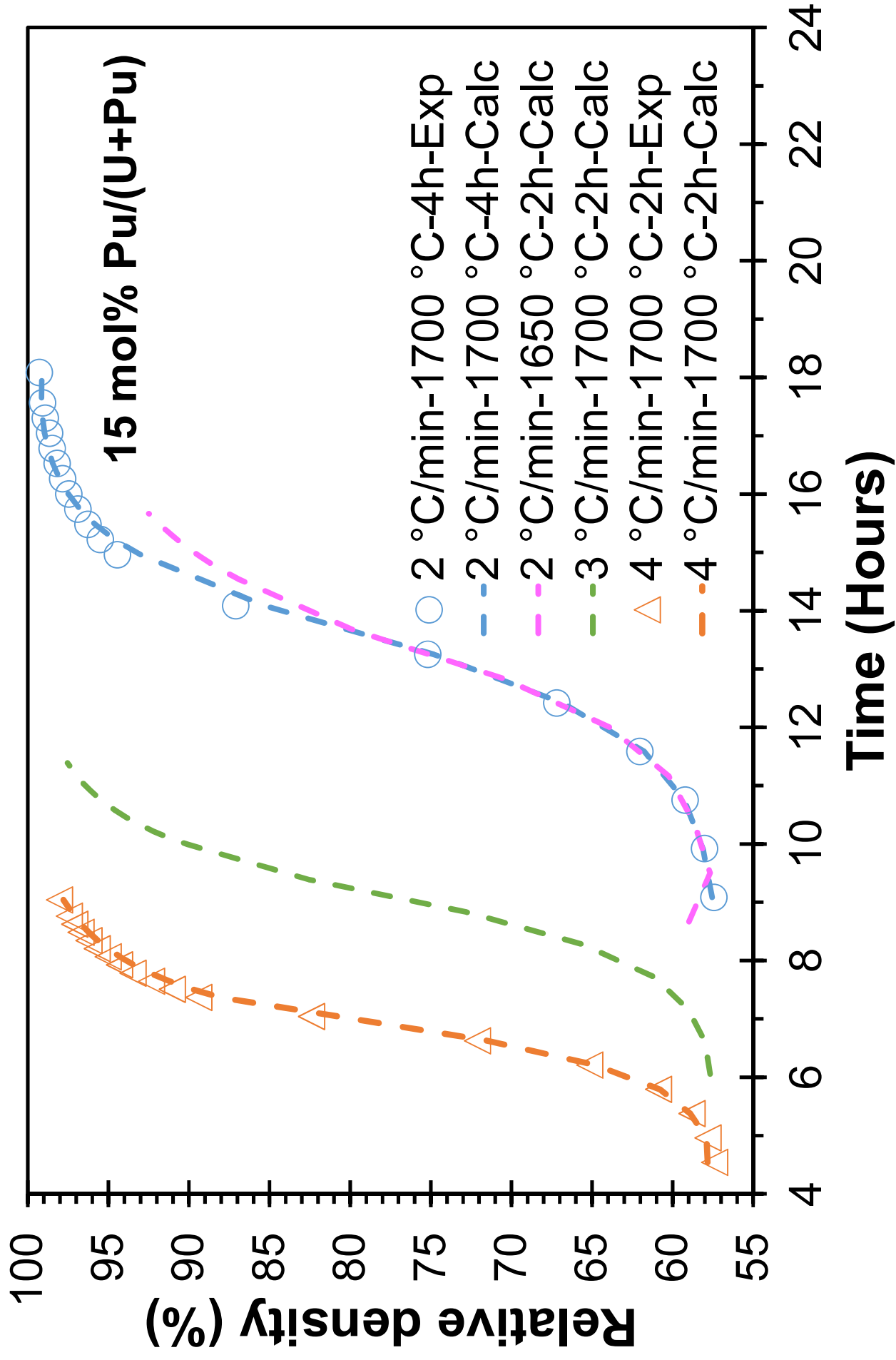


Fig8

